



An Immersed Boundary Method for flows with evaporating droplets

Giandomenico Lupo^{a,*}, Mehdi Niazi Ardekani^a, Luca Brandt^{a,b}, Christophe Duwig^a

^aLinné Flow Center and SeRC (Swedish e-Science Research Centre), Department of Mechanics, Royal Institute of Technology (KTH), Sweden

^bDepartment of Energy and Process Engineering, Norwegian University of Science and Technology (NTNU), Norway

ARTICLE INFO

Article history:

Received 24 January 2019

Received in revised form 31 July 2019

Accepted 10 August 2019

Keywords:

Spray

Fuel

Evaporation

Phase change

Immersed boundary

Multiphase

Direct numerical simulation

ABSTRACT

We present a new Immersed Boundary Method (IBM) for the interface resolved simulation of spherical droplet evaporation in gas flow. The method is based on the direct numerical simulation of the coupled momentum, energy and species transport in the gas phase, while the exchange of these quantities with the liquid phase is handled through global mass, energy and momentum balances for each droplet. This approach, applicable in the limit of small spherical droplets, allows for accurate and efficient phase coupling without direct solution of the liquid phase fields, thus saving computational cost. We provide validation results, showing that all the relevant physical phenomena and their interactions are correctly captured, both for laminar and turbulent gas flow. Test cases include fixed rate and free evaporation of a static droplet, displacement of a droplet by Stefan flow, and evaporation of a hydrocarbon droplet in homogeneous isotropic turbulence. The latter case is validated against experimental data, showing the feasibility of the method towards the treatment of conditions representative of real life spray fuel applications.

© 2019 Elsevier Ltd. All rights reserved.

1. Introduction

Evaporating sprays occur frequently in nature (e.g. falling rain, fog, breathing in living organisms) and are a key feature of many engineering applications, such as aerosols, wet scrubbers, water curtains, spray dryers and most importantly combustion systems. Regarding the latter, the evaporation dynamics of the spray droplets are of crucial importance in most burner designs. For example spray evaporation affects significantly the performance of lean pre-vaporized premixed (LPP) burners in gas turbines, in terms of efficiency and pollutant emissions [1].

The evaporation of multiple droplets is a multicomponent multiphase flow with strong interaction of mass, momentum and heat transport. The ability to understand and accurately describe the complex interplay of these phenomena is of prime importance. Traditional methods for the numerical simulation of such flows treat the spray as a collection of material points [2,3], relying on models for the exchange of physical quantities between continuous and dispersed phase. This approach is prevalent even in recent studies [4–7], due to computational efficiency, but the models leave out the more complex coupling of physical phenomena. Furthermore, model parameters are known to have a significant impact on the simulation results. Interface resolved numerical

simulations, on the other hand, are ideally able to capture all the relevant phenomena with little to no modelling apart from basic assumptions.

Interface resolved numerical methods for multiphase flow fall into two main categories, depending on the treatment of the moving boundary: interface tracking methods and interface capturing methods. In interface tracking methods, the interface is explicitly described by the computational mesh, either in a Eulerian-Eulerian framework by a moving mesh that conforms to the interface [8,9], or in a Eulerian-Lagrangian framework by a separate Lagrangian mesh that tracks the interface on top of the underlying Eulerian mesh [10,11]. These methods provide great accuracy in the description of the interface shape and curvature, but lack robustness in cases of large interface deformation. In interface capturing methods, the interface is represented by a scalar field which is transported in the same way as the physical variables. Examples are the Volume of Fluid method (VOF) [12,13] and the Level Set method [14,15]. While the interface capturing approach allows for treatment of phenomena where the interface undergoes severe deformation and even topological change (e.g. phase breakup and coalescence), details of the interface shape such as curvature need to be artificially reconstructed, making these methods less suitable for problems where such details are important, with possible errors in mass conservation between the fluid phases.

The Lattice Boltzmann method (LBM) has been recently used to simulate multiphase flows with phase change [16,17]. It employs

* Corresponding author.

E-mail address: gianlupo@mech.kth.se (G. Lupo).

mesoscopic kinetic equations for fluid pseudoparticles embedded in a regular lattice, instead of macroscopic transport equations discretized on a computational grid. This framework is particularly convenient for the description of the phase boundary as a diffuse interface [18,19].

All methods discussed above describe the flow fields in all fluid phases, as well as the interface deformation. For flows where the two fluid phases can be characterized as a continuous phase and a dispersed phase, the latter consisting of a large number of individual droplets (i.e. evaporating sprays), the computational cost of the methods described above soon becomes unaffordable, as the interfacial area approximately grows with the cubic root of the droplet number. On the other hand, in many instances the details of the interface deformation and flow inside the dispersed phase are not relevant (e.g. spray droplets with small Weber number). Taking advantage of this, we propose an efficient Immersed Boundary Method (IBM) tailored for the simulation of spherical droplet evaporation, which can be extended to tackle other multiphase flows with phase change. IBMs are a class of Eulerian-Lagrangian interface tracking methods [20,21], whose most attractive feature is the use of a simple Cartesian mesh for the flow discretization. This allows to handle complicated boundary geometries in an efficient and straightforward way, and lends itself naturally to continuous-dispersed multiphase flows. In this field, the method originally proposed by Uhlmann [22] and improved by Breugem [23] has been particularly successful in direct numerical simulation of particle laden flows [24–26], and has been extended by Ardekani et al. [27] to treat heat transfer. In this paper we develop it further to include species mass transfer together with phase change. The focus is on capturing the relevant features of multiphase flows with phase change at an interface resolved level, without direct solution of the fields inside the dispersed phase, and eschewing the description of the interface deformation by a priori assumption of the interface shape. The benefits of this approach are robustness and low computational cost, without loss of accuracy in the description of the phase change dynamics.

After laying out the mathematical formulation of the problem and discussing its assumptions in Section 2, we present the numerical method in Section 3. Section 4 is dedicated to the results of four test cases that provide the verification and validation for the method.

2. Mathematical formulation

We focus on the vaporization of small liquid droplets in a gas flow. The nondimensional parameters that characterize the system are summarized in Table 1. In addition to these, one or more dimensional parameters are introduced by the vapour-liquid equilibrium relation, which also requires the molecular weights of the vapour and inert gas components ($M_{w,vapour}$ and $M_{w,inert}$) and the prescription of the total thermodynamic pressure \hat{P}_{tot} .

2.1. Assumptions

We first clarify the method assumptions, and discuss their validity and range of applicability.

- (A1) All physical and transport properties are constant.
- (A2) The flow is incompressible.
- (A3) Gravity is neglected.
- (A4) Droplets remain spherical.
- (A5) The fluid motion inside the droplets is neglected.
- (A6) Temperature is uniform on the droplet surface.
- (A7) The gas phase is ideal.
- (A8) The inert gas is insoluble in the liquid phase.

Table 1
Characteristic non-dimensional parameters.

| Parameter | Definition | Description |
|---------------------|--|---|
| Re | $\frac{\hat{U}_g \hat{r}_0}{\hat{\nu}}$ | Reynolds number |
| Pr | $\frac{\hat{\nu}}{\hat{\alpha}}$ | Prandtl number |
| Sc | $\frac{\hat{\nu}}{\hat{D}}$ | Schmidt number |
| ϕ_ρ | $\frac{\hat{\rho}_l}{\hat{\rho}}$ | Liquid to gas density ratio |
| ϕ_{c_p} | $\frac{\hat{c}_{pl}}{\hat{c}_p}$ | Liquid to gas specific heat ratio |
| ϕ_α | $\frac{\hat{\alpha}_l}{\hat{\alpha}}$ | Liquid to gas heat diffusivity ratio |
| $\phi_{c_p,vap}$ | $\frac{\hat{c}_{p,vapour}}{\hat{c}_p}$ | Vapour to gas specific heat ratio |
| $\phi_{\Delta c_p}$ | $\frac{\hat{c}_{p,vapour} - \hat{c}_{p,inert}}{\hat{c}_p}$ | Differential heat capacity in the gas mixture |
| Ste | $\frac{\hat{c}_{pl} \hat{T}^*}{\hat{\lambda}_l}$ | Stefan number |

- (A9) Thermodynamic equilibrium prevails at the droplet surface.
- (A10) The surface tension effect on vapour pressure (Kelvin effect) is neglected.
- (A11) The viscous dissipation term is neglected.
- (A12) Soret and Dufour effects are neglected.

The Assumption A1 of constant properties is justified in the case of relatively small temperature excursions, as for the validation cases presented in the current paper. It is however easily relaxed should the need arise. The dependence of the properties on composition should not be underestimated, especially with regard to the liquid phase, since it becomes notably significant in multicomponent evaporation, as shown in Hubbard et al. [28], Kneer et al. [29], Lupo and Duwig [30].

The incompressibility Assumption A2 effectively decouples the mechanical and thermodynamic pressure, leaving the latter as a degree of freedom of the system. While compressibility effects on the flow itself are generally negligible in the range of conditions where most spray applications operate (i.e. low Mach number), mass transport is driven by thermodynamic partial pressure gradients in the gas, as opposed to momentum transport which in an incompressible framework is associated with gradients of mechanical pressure. Compressibility effects on phase change are especially relevant in case of flash evaporation, which Assumption A2 thus excludes from the scope of our method.

Effects of gravity are out of the scope of the present work (Assumption A3); for applications where they are relevant they can be easily introduced in our current framework as a body force acting on the dispersed phase [31], and as a buoyancy term in the continuous phase via Boussinesq approximation. Buoyancy inside the dispersed liquid phase is neglected. For hydrocarbon fuel spray evaporation the Rayleigh number¹ is of the order of $Ra \sim 5 \times 10^{-2}$, thus buoyancy driven internal circulation is unimportant. The effect can be relevant in multicomponent droplet vaporization at very high temperatures [32].

Assumption A4 relies on the fact that droplets are small enough to resist deformation and breakup by inertia and shear. Deformation is not substantial as long as $We \ll 1$, while the critical Weber number² for breakup is usually reported as $We = 12$ [33]. After secondary breakup, typical Weber numbers for fuel spray combustion

¹ The Rayleigh number is defined as $Ra = \frac{\Delta \rho_l g r_0^3}{\alpha_l \mu_l}$.

² The Weber number is defined as $We = \frac{2 \rho_l \hat{U}_g \hat{r}_0}{\sigma_l}$.

are in the range $0.1 < We < 16$ [34]. While seemingly wide, the simultaneous evaporation reduces the Weber number continuously, effectively competing with deformation and breakup. It is then important to evaluate the respective time scales. In typical combustion engine and gas turbine applications the evaporation time scale is of the order of $\hat{t}_{ev} \sim 1 \times 10^{-3}$ s, while the breakup time scale³ is in the range 1×10^{-4} s $< \hat{t}_b < 1 \times 10^{-3}$ s [34]. This indicates that a wide range of scenarios is indeed characteristic for the spray droplets during evaporation and combustion. However, the evaporation dynamics are governed by the available liquid-gas interface; hence evaporation is not significantly altered provided that the shape deformation does not heavily modify the specific surface area of the droplet, as will be demonstrated in Section 4.4.

Assumptions A5 and A6 require that heat transport inside the droplet is fast compared to the rate at which the droplet receives heat from the surrounding gas, i.e. the Biot number⁴ is small. This is estimated as $0.1 < Bi < 1.5$ for fuel droplets up to 1 mm of diameter, see the 1D evaporation model in Lupu and Duwig [30].

The ideal gas Assumption A7 has no bearing on the fluid dynamics, as the flow is incompressible, but prescribes unity fugacity coefficients in the vapour-liquid equilibrium. This is acceptable at low gas pressures. For evaporation of droplets in a high pressure environment the assumption might not be valid [35], and fugacity models must be introduced in the vapour-liquid equilibrium.

At the relatively high temperatures we consider in our study, the solubility of nitrogen or air in water or fuel liquids is very low, so A8 is a fair approximation.

The Kelvin effect A10 was found to be negligible for the present study: vapour pressure is only enhanced by around 0.2% for a $d_{s0} = 1$ m fuel droplet.

Viscous heating is also insignificant in our framework (A11), as the gas environment is already hot: the Brinkman number⁵ is of order $Br \sim 10^{-7}$.

Lastly, neglecting thermophoresis (A12) is acceptable as the Soret coefficient is of the order $S_T = \frac{D_{Soret}}{D} \sim 10^{-5} \div 10^{-3} K^{-1}$ [36], and the highest temperature differences we consider are of the order $\Delta T \sim 10^2$ K. The reciprocal phenomenon, that is heat flux due to a composition gradient (Dufour effect), is expected to be comparable, considering that $D_{Dufour} = D_{Soret}$ by Onsager reciprocal relations [36], and that $Le \sim 1$ in most applications.

2.2. Gas phase

The equations describing the gas phase (momentum, heat and species transport), in their nondimensional form, read:

$$\nabla \cdot \mathbf{u} = 0; (1a)$$

$$\frac{\partial \mathbf{u}}{\partial t} = -\mathbf{u} \cdot \nabla \mathbf{u} - \nabla p + \frac{1}{Re} \nabla^2 \mathbf{u}; (1b)$$

$$\frac{\partial T}{\partial t} = -\mathbf{u} \cdot \nabla T + \frac{1}{RePr} \nabla^2 T + \frac{\phi_{\Delta Cp}}{ReSc} \nabla T \cdot \nabla Y; (2)$$

$$\frac{\partial Y}{\partial t} = -\mathbf{u} \cdot \nabla Y + \frac{1}{ReSc} \nabla^2 Y; (3)$$

³ The breakup time scale in absence of viscous damping is approximately $\hat{t}_b \sim 10 \frac{r_{s0}}{|U_l - U_g|} \sqrt{\phi_\rho}$. Viscous effects dominate when the Ohnesorge number

$Oh = \frac{\mu_l}{\sqrt{2\rho_l \sigma r_{s0}}}$ is large, but in fuel spray applications typically $Oh < 0.1$.

⁴ The Biot number is defined as $Bi = \frac{\hat{q}}{2\pi r_{s0} k (\hat{T}_\infty - \hat{T}_s)}$.

⁵ The Brinkman number is defined as $Br = \frac{\mu_l \hat{U}_l - \hat{U}_g^2}{k (\hat{T}_\infty - \hat{T}_s)}$.

The Assumption A4 of droplet sphericity means that no surface tension term is added to the RHS of Eq. (1) directly. Instead, the IBM force field, active in the vicinity of the interface, accounts indirectly for the surface tension force that preserves the spherical shape. Numerically, this is advantageous as large surface tension forces, arising in droplets with low capillary numbers, introduce an additional stability constraint to the time integration scheme.

The last term on the RHS of Eq. (2) is the net enthalpy flux resulting from the different heat capacities that the vapour and inert gas carry as they diffuse into each other (see Appendix A for a derivation). It has been shown to be of importance in the prediction of evaporation rates of spherical droplets in a stagnant gas environment [30].

2.3. Liquid phase

In our framework we are not interested in solving the flow inside the dispersed phase, but only consider the global mass, momentum and energy exchange between the dispersed and continuous phase. In the limit of small Biot numbers, an infinite conductivity assumption in the liquid phase is justified, so that at each instant a droplet has uniform temperature ($\hat{T}_l = \hat{T}_s$). The heat balance for the droplet is then:

$$\rho_l C_{pl} \frac{d\hat{T}_s}{dt} = -\frac{3(\hat{q} + \hat{m}\Lambda)}{4\pi r_s^3}; (4)$$

where $(\hat{q} + \hat{m}\Lambda)$ is the sensible heat entering the droplet (i.e. total minus latent). The simplification may be not valid when the Biot number is of order unity or larger. However, this is usually the case for big droplets, for which the evaporation time scale is slow and the heat conduction in the liquid can be solved analytically (Eq. (B.9) in Appendix B). The liquid temperature profile can then be averaged to give:

$$\hat{T}_l(\hat{t}) = \hat{T}_s(\hat{t}) + \sum_{n=1}^{\infty} \frac{6}{(n\pi)^2} (\hat{T}_0 - \hat{T}_s(\hat{t})) e^{-\alpha_n^2(\hat{t})\hat{t}}; (5)$$

Substitution into Eq. (4) gives a new equation for the evolution of the surface temperature, which is used to predict more accurately the thermodynamic equilibrium at the surface when the Biot number is of order unity, preserving computational efficiency.

In their nondimensional form, the global balances for each droplet are therefore the mass balance (droplet radius equation):

$$\frac{dr_s}{dt} = -\frac{\hat{m}}{4\pi r_s^2 \phi_\rho}; (6)$$

and the energy balance (droplet temperature equation) rewritten as:

$$\frac{dT_s}{dt} = \frac{\frac{6}{RePr} \phi_\alpha (T_0 - T_s) \left(\frac{1}{r_s^2} - \frac{2}{r_s} \frac{dr_s}{dt} t \right) \sum_{n=1}^{\infty} e^{-\frac{1}{RePr} \left(\frac{n\pi}{r_s} \right)^2 \phi_\alpha t} - \frac{3 \left(\frac{\hat{q}}{\phi_{cp}} + \frac{\hat{m}}{Stc} \right)}{4\pi r_s^3 \phi_\rho}}{1 - \sum_{n=1}^{\infty} \frac{6}{(n\pi)^2} e^{-\frac{1}{RePr} \left(\frac{n\pi}{r_s} \right)^2 \phi_\alpha t}}; (7)$$

In the presence of strong convective currents, the liquid circulation can significantly enhance the heat transfer in the liquid [37]. This effect can be taken into account by increasing the effective liquid heat diffusivity, multiplying the parameter ϕ_α by a factor χ , as defined in Eq. (39) of [2].

2.4. Phase coupling, boundary conditions and vapour-liquid equilibrium

The coupling between the liquid and gas phase is realized through the boundary conditions on the droplet surface on the

gas side and the prescription of the nondimensional heat and mass transfer rates \tilde{q} and \tilde{m} .

The gas-liquid interface of an evaporating droplet is a discontinuity across which mass, momentum and energy are conserved. The quantities on the two sides of the interface are related by the Rankine-Hugoniot conditions [38]. Mass conservation gives:

$$\mathbf{u} = \mathbf{u}_c - \left(\phi_\rho - 1\right) \frac{dr_s}{dt} \mathbf{n}; \quad \text{for } |\mathbf{x} - \mathbf{x}_p| = r_s. \quad (8)$$

This is the boundary condition on velocity on the gas side, where \mathbf{x}_p is the interface position, and \mathbf{n} is the outward pointing unit vector normal to the droplet surface. Calculation of \mathbf{n} is made trivial by the assumption of droplet sphericity, as it's determined entirely by the position \mathbf{x}_c of the droplet centroid:

$$\mathbf{n} = \frac{\mathbf{x}_p - \mathbf{x}_c}{|\mathbf{x}_p - \mathbf{x}_c|}. \quad (9)$$

Similarly, since the droplet moves rigidly, and we are not concerned with the fluid motion in the liquid, the liquid phase velocity \mathbf{u}_c is the velocity of the droplet centroid, which is calculated by lagrangian tracking of each droplet. The Rankine-Hugoniot condition on momentum would involve the balance between surface tension, pressure, viscous stress and phase change momentum, but it is made redundant by Assumption A4, as the momentum exchange between the gas and the liquid phase is limited to the droplet rigid motion. The same assumption, together with the incompressibility Assumption A2, removes the need for the Rankine-Hugoniot condition on energy, as the energy coupling of the phases is fully determined via continuity of the temperature and thermodynamic equilibrium.

The nondimensional heat and mass transfer rates are specified by integrating the fluxes over the droplet surface $S(t)$:

$$\tilde{m} = \int_S \left(-\frac{1}{ReSc} \nabla Y + \mathbf{u} Y \right) \cdot \mathbf{n} dS. \quad (10)$$

$$\tilde{q} = \int_S \left(-\frac{1}{RePr} \nabla T \right) \cdot \mathbf{n} dS. \quad (11)$$

where their sign is relative to \mathbf{n} , allowing the set of governing equations to be consistent for both evaporation and condensation.

The boundary condition for temperature is obtained by imposing continuity across the liquid and gas phase:

$$T = T_s; \quad \text{for } |\mathbf{x} - \mathbf{x}_p| = r_s. \quad (12)$$

The boundary condition for the vapour mass fraction comes from the hypothesis of thermodynamic equilibrium, which relates the gas molar composition to the liquid surface temperature:

$$\begin{cases} \tilde{Y}_s = \frac{\hat{p}_{vapour}^{sat}(T_s)}{\hat{P}_{tot}}; \\ Y_s = \frac{\tilde{Y}_s M_{w,vapour}}{(1-\tilde{Y}_s)M_{w,inert} + \tilde{Y}_s M_{w,vapour}}; \end{cases} \quad \text{for } |\mathbf{x} - \mathbf{x}_p| = r_s. \quad (13)$$

The expression for the vapour pressure $\hat{P}_{vapour}^{sat}(\hat{T})$ can be chosen according to the nature of the liquid that is vaporizing. Depending on this choice, one or more additional parameters are introduced in the problem, hence we retain dimensional quantities for the vapour-liquid equilibrium. The total thermodynamic pressure \hat{P}_{tot} also needs to be specified. Many evaporation models assume that the total pressure at the droplet surface is equal to the inert gas pressure and is constant [3]: $\hat{P}_{tot} = \hat{P}_{inert}$, i.e. the evaporation is isobaric. However, as the droplet temperature tends to the boiling point at the prevailing pressure, i.e. $\hat{P}_{vapour}^{sat}(\hat{T}_s) \rightarrow \hat{P}_{inert}$ and $Y_s \rightarrow 1$, the evaporation rate calculated by

Eq. (10) becomes singular. This shortcoming can be circumvented by assuming that the evaporation is isochoric, which leads to $\hat{P}_{tot} = \hat{P}_{vapour}^{sat}(\hat{T}_s) + \hat{P}_{inert}$, and is used in the present work. However we must remark that the isochoric assumption is in contrast with the incompressibility assumption for the fluid flow, and therefore is only acceptable for moderate values of the vapour pressure. In fact, flash vaporization and boiling, which occur in very high temperature environments, can be treated as isobaric by replacing Eq. (10) with:

$$\tilde{m} = \tilde{q} \frac{Ste}{\phi_{cp}}. \quad (14)$$

This is known as kinetic vaporization regime [39], as the driving force for the phase change is the surface temperature gradient, rather than the vapour concentration gradient of Eq. (10) (diffusional vaporization regime). Although the present work focuses on evaporation proper (i.e. diffusional), the kinetic formulation is easily implemented in our framework and can be used to treat flash vaporization cases, or combined with the diffusional formulation for mixed evaporation/boiling problems like the Leidenfrost effect [40].

2.5. Lagrangian droplet tracking

Each droplet moves rigidly in the continuous phase according to the (nondimensional) Newton-Euler Lagrangian equations:

$$\frac{d\mathbf{u}_c}{dt} = \frac{3}{4\pi\phi_\rho r_s^3} \int_S \left(-p\mathbf{I} + \frac{1}{Re} (\nabla\mathbf{u} + \nabla\mathbf{u}^T) \right) \cdot \mathbf{n} dS \quad (15)$$

$$\frac{d\boldsymbol{\omega}_c}{dt} = \frac{15}{8\pi\phi_\rho r_s^5} \int_S (r_s\mathbf{n}) \times \left(-p\mathbf{I} + \frac{1}{Re} (\nabla\mathbf{u} + \nabla\mathbf{u}^T) \right) \cdot \mathbf{n} dS \quad (16)$$

where \mathbf{u}_c and $\boldsymbol{\omega}_c$ are the linear and angular velocity of the droplet centroid. The right hand sides of Eqs. (15) and (16) represent the hydrodynamic force and torque exerted on the droplet by the surrounding fluid. These are fully resolved, so that hydrodynamic-mediated modulations of momentum, heat and mass transfer in the continuous phase are captured directly. The droplet radius r_s in Eqs. (15) and (16) is not constant as droplets change in size due to phase change.

3. Numerical method

The present Immersed Boundary Method (IBM) is based on the one developed by Breugem [23] for solving particle laden turbulent flows. Its key concept is to solve the continuous phase on a fixed Cartesian staggered uniform ($\Delta x = \Delta y = \Delta z$) grid (Eulerian Mesh), while a separate grid is attached to and moves with the surface of the dispersed phase (Lagrangian Mesh) (Fig. 1a).

A flowchart of the algorithm used to advance the solution from time step n to time step $n+1$ is shown in Figs. 2 and 3. Time integration is performed by a three-step Runge-Kutta scheme (iterations denoted by the index q in Fig. 2). The Runge-Kutta coefficients are $\alpha_1 = \frac{32}{60}; \beta_1 = 0; \alpha_2 = \frac{25}{60}; \beta_2 = -\frac{17}{60}; \alpha_3 = \frac{45}{60}; \beta_3 = -\frac{25}{60}$. Spatial discretization on the Eulerian Mesh is performed with a second order central differencing scheme. A pressure correction-scheme is used to solve the Navier-Stokes equation, as shown in Eqs. (17a) and (17r) to (17t). The term \mathbf{rhs}_u in Eq. (17a) represents the right hand side of Eq. (1) excluding the pressure gradient. The terms $\mathbf{rhs}_T, \mathbf{rhs}_Y, \mathbf{rhs}_{r_s}, \mathbf{rhs}_{T_s}, \mathbf{rhs}_{u_c}$ and \mathbf{rhs}_{ω_c} in Eqs. (17b), (17c), (17w), (17d), (17x) and (17y) represent the right hand sides of Eqs. (2), (3), (6), (7), (15) and (16) respectively.

The Eulerian Mesh does not conform to the continuous-dispersed interface (the droplet surface), so the boundary conditions on the interface cannot be imposed directly. Instead, they are mimicked by equivalent force fields (\mathbf{f}_u, f_T and f_Y in Eqs.

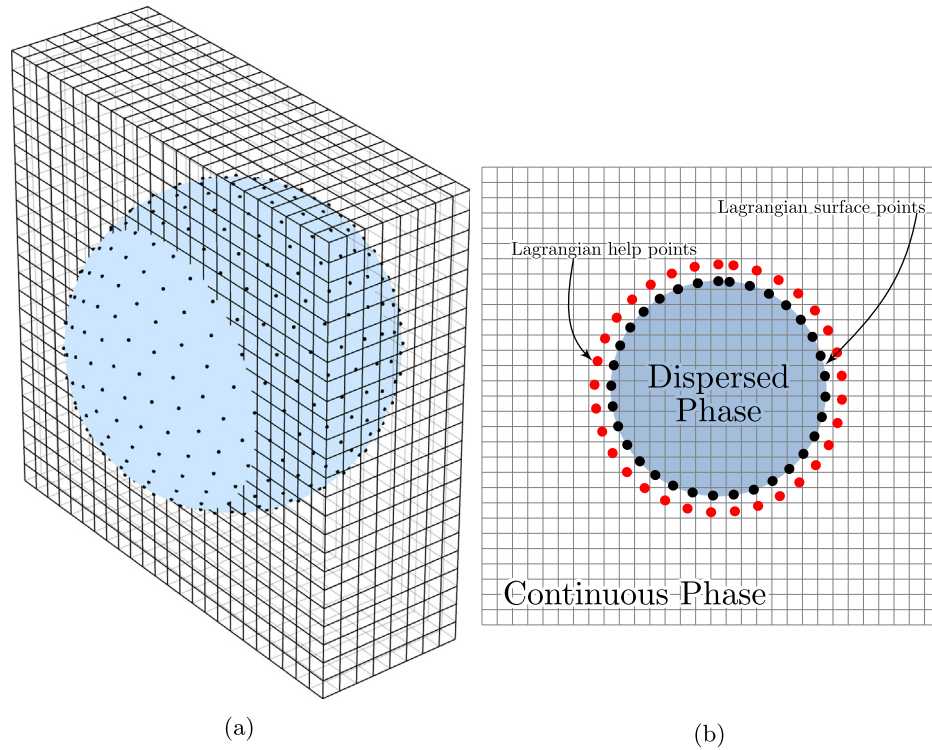


Fig. 1. Illustration of the Eulerian and Lagrangian Mesh used to solve the continuous and dispersed phase. (a) Distribution of Lagrangian grid points over the interface. (b) The Eulerian cells belonging to the continuous phase and the dispersed phase are marked in white and blue respectively. Lagrangian help points used to compute surface gradients are marked in red. (For interpretation of the references to colour in this figure legend, the reader is referred to the web version of this article.)

(17l), (17m), (17n)) added to the right-hand side of each continuous phase transport equation after discretization (this approach is known as discrete forcing immersed boundary [21]). These forces must be active only in the immediate vicinity of the immersed boundary, therefore they are calculated on the points \mathbf{X}_l of the Lagrangian Mesh (as \mathbf{F}_u, F_T and F_Y in Eqs. (17i), (17j), (17k)) and then spread to the neighbouring cells of the Eulerian Mesh by means of the regularized Dirac delta function δ_d proposed by Roma et al. [41]. The same function δ_d is used to interpolate the Eulerian fields onto the Lagrangian interface points. The velocity boundary condition $\mathbf{u}(\mathbf{X}_l)$ is evaluated from Eq. (8). The computation of the discrete forces on the boundary is performed iteratively (Eqs. (17f)–(17q), with iterations denoted by the index s) in order to better enforce the desired boundary condition. The number of iterations is set to $N_s = 3$.

We point out that the volume of the Lagrangian cell ΔV_l is not constant, since the dispersed phase is changing size due to the phase change. For droplet evaporation/condensation:

$$\Delta V_l = \frac{\frac{4}{3}\pi \left[\left(r_s + \frac{\Delta x}{2} \right)^3 - \left(r_s - \frac{\Delta x}{2} \right)^3 \right]}{N_l}; \quad (18)$$

where r_s is the droplet radius and N_l is the number of Lagrangian points on the droplet surface.

The distinctive feature of the evaporation problem lies in the fact that the continuous-dispersed interface acts as a velocity inlet (see Eq. (8)), injecting mass in the continuous phase domain. In the IBM framework the continuous-dispersed interface is an array of points immersed in the continuous phase (Fig. 1b). Therefore the computational domain of the continuous phase is not simply connected, and the velocity inlet from the interface is implemented as a mass source. The source is generated by a positive velocity divergence s_U in a suitable portion of the volume enclosed by the interface, which is directly added to the right hand side of the Poisson equation for the pressure correction \tilde{p} (Eq. (17r)). The amplitude

of the mass source must be equal to the evaporation rate (Eq. (10)) divided by the chosen source volume. In order to obtain a smooth velocity field across the interface, the source term is distributed inside the droplet volume as to produce a velocity divergence that goes smoothly to zero for $r \rightarrow r_s$:

$$s_{ijk,U} = \begin{cases} -3 \frac{dr_s}{dt} \frac{\phi_\rho}{r_s} \frac{(1 + \cos(\frac{\pi r_{ijk}}{r_s}))}{(1 - \frac{6}{\pi^2})}; & \text{for } r_{ijk} \leq r_s; \\ 0; & \text{for } r_{ijk} > r_s; \end{cases} \quad (19)$$

where $r_{ijk} = |\mathbf{x}_{ijk} - \mathbf{X}_c|$.

Calculation of the terms rhs_{r_s} and rhs_{T_s} in Eqs. (17w) and (17d) involves the evaluation of the mass and heat transfer rates \dot{m} and \dot{q} by Eqs. (10) and (11). To this end the normal components of the temperature and vapour mass fraction gradient at the interface are needed. We therefore introduce an additional layer of Lagrangian help points located on a spherical shell of radius $\left[\frac{r_s}{r_{s0}} (r_s + \Delta x) \right]$, as shown in Fig. 1b. Each help point is used together with the corresponding Lagrangian point on the interface for a first order approximation of the normal gradient:

$$[\nabla T \cdot \mathbf{n}]_{\mathbf{x}=\mathbf{X}_l} \approx \frac{T_l^h - T_s}{\Delta x}. \quad (20)$$

$$[\nabla Y \cdot \mathbf{n}]_{\mathbf{x}=\mathbf{X}_l} \approx \frac{Y_l^h - Y_s}{\Delta x}. \quad (21)$$

The values of the temperature T_l^h and vapour mass fraction Y_l^h on the Lagrangian help point are calculated by interpolation from the neighbouring Eulerian cells using the aforementioned δ_d function (as is Eqs. (17g) and (17h)).

As done for mass in Eq. (19), source terms of energy and species, originating from the vaporizing mass, are distributed inside the droplet volume, and added to Eqs. (17b) and (17c):

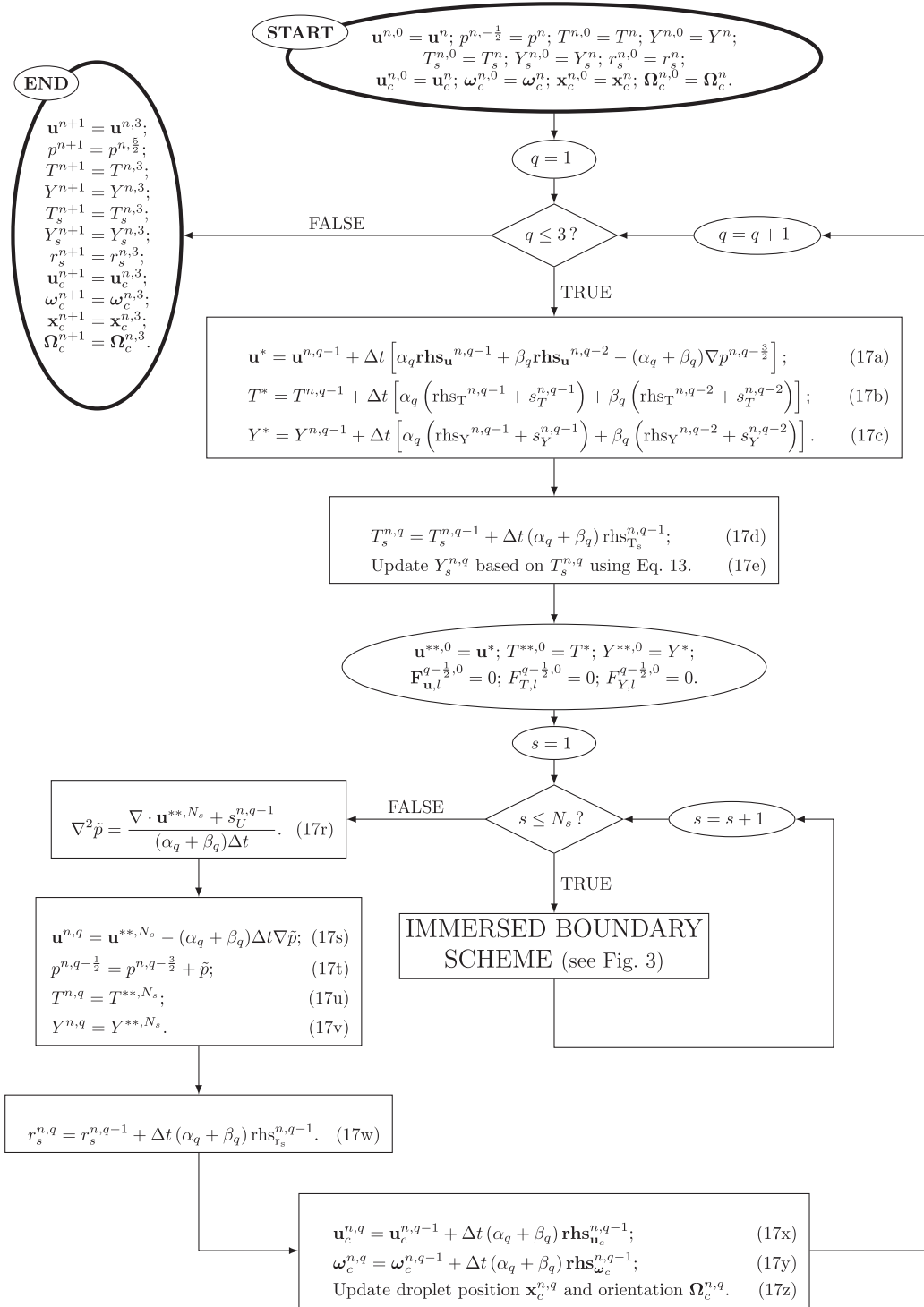


Fig. 2. Flowchart of the numerical scheme for advancing the flow solution from step n to step $n + 1$.

$$s_T = s_U (1 - \phi_{c,p,vap}) T; \quad (22)$$

$$s_Y = s_U. \quad (23)$$

Calculation of $\mathbf{rhs}_{\mathbf{u}_c}$ and $\mathbf{rhs}_{\boldsymbol{\omega}_c}$ in Eqs. (17x) and (17y) involves the evaluation of the hydrodynamic force and torque exerted by the continuous fluid on the dispersed phase, as explained in detail by Breugem [23].

4. Verification and validation

Four test cases were chosen in order to verify and validate the method in a progressive fashion, by successively increasing the physical complexity. In the first case we prescribe the evaporation rate of a static droplet, calculating the Stefan flow around it in order to verify the correct coupling between phase change and gas momentum transport. The evaporation rate is freely driven

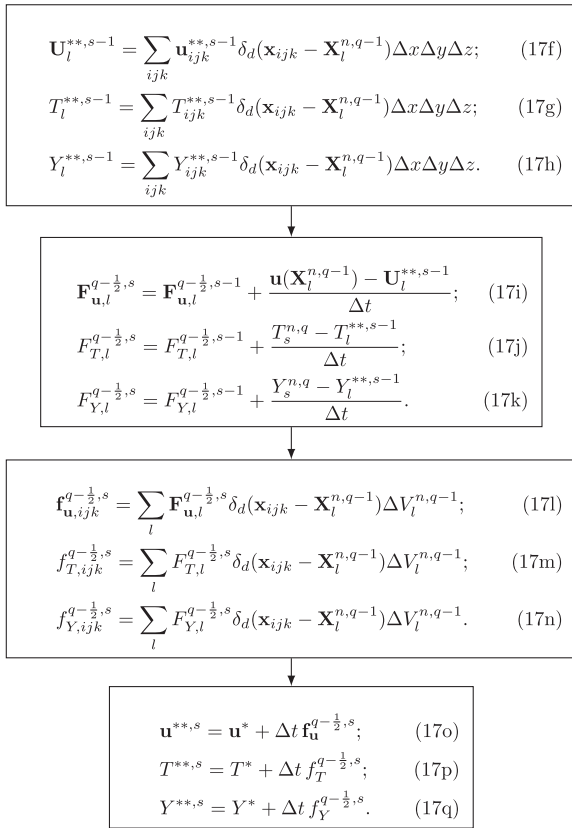


Fig. 3. Detailed flowchart of the immersed boundary scheme of Fig. 2.

by temperature and composition gradients in the second case, thus verifying the correct coupling between thermodynamics, phase change, and gas heat, species and momentum transport. In the third case, we allow the droplet to be displaced by the Stefan velocity, in order to verify the correct momentum exchange between the two phases. Finally, the fourth case reproduces the evaporation of a hydrocarbon droplet in homogeneous isotropic turbulence, verifying the method under turbulent flow conditions. Comparison with experimental data provides validation for conditions that are representative of real life spray fuel applications. The parameters used are summarized in Table 2. In the first three cases the computational domain is a cube with $L_x = L_y = L_z = 8r_{s0}$, discretized with

and Eulerian Mesh of $(128 \times 128 \times 128)$ cells. In the fourth case the computational domain is a cube of size $L_x = L_y = L_z = 21.32 r_{s0}$, and Eulerian Mesh of $(384 \times 384 \times 384)$ cells. The initial droplet diameter is resolved by 32 Eulerian cells for cases 1–3, by 36 Eulerian cells for case 4.

4.1. Case 1. Evaporation of a static droplet at a fixed rate

The droplet is fixed at the centre of the domain and vaporizes at a fixed rate, by imposing a constant radius regression speed $\frac{dr_s}{dt} = -c$; energy and species transport are turned off. In this case $c = 10^{-4}$. The analytical velocity field in the gas phase is purely radial and decays with the radius squared:

$$u_r(r, t) = -c \left(1 - \phi_\rho\right) \left(\frac{r_s(t)}{r}\right)^2. \quad (24)$$

This is verified in Fig. 4. The discrepancy between the profiles calculated near the outer boundary is due to the uniform boundary conditions on the limits of the cubic computational box, which break the spherical symmetry. However, as the evolution of the droplet depends on the heat and mass flux at the interface, the exact outer boundary condition is not important as long as it does not affect the ability to correctly predict the gradients at the interface.

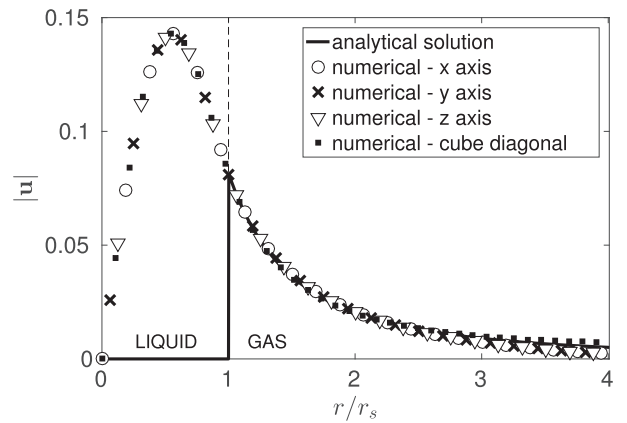


Fig. 4. Non dimensional velocity profiles generated by a droplet evaporating at constant radius regression speed. Profiles along the principal axes of the Cartesian mesh and along the cube diagonal of the computational box are shown.

Table 2
Parameters for test cases 1, 2, 3 and 4.

| Case | Re | Pr | Sc | ϕ_ρ | ϕ_{c_p} | $\phi_{\Delta c_p}$ | ϕ_α | Ste |
|-------------|--|--------------------|-----------------------|------------------------|------------------------|---------------------|------------------------|--------|
| 1 | 1 | – | – | 815.66 | – | – | – | – |
| 2 | 1 | 0.7899 | 1.6326 | 692.2 | 1.758 | 0.98 | 2.82×10^{-3} | 1.98 |
| 3 | 1 | 0.387 | 0.726 | 10 | 2 | 0 | 3.826×10^{-3} | 1.04 |
| 4 (heptane) | (4a) 570 (4b) 504.6 (4c) 577.3 (4d) 579.8 | 0.7516 | 1.75 | 515.4 | 2.03 | 0.5872 | 4.8×10^{-3} | 1.8529 |
| 4 (decane) | (4a) 570 (4b) 504.6 (4c) 577.3 (4d) 579.8 | 0.7248 | 2.6544 | 632.38 | 2.1214 | 0.566 | 1.9×10^{-3} | 1.8447 |
| Case | \hat{T}_∞ [K] | \hat{T}_{10} [K] | $M_{w,inert}$ [g/mol] | $M_{w,vapour}$ [g/mol] | \hat{P}_{inert} [Pa] | | | |
| 1 | – | – | 28 | 18 | – | | | |
| 2 | 741 | 342.85 | 28 | 100 | 101325 | | | |
| 3 | 1073 | 353 | 28 | 18 | 101325 | | | |
| 4 (heptane) | 298.15 | 285.56 | 28 | 100 | 101325 | | | |
| 4 (decane) | 298.15 | 297.73 | 28 | 142 | 101325 | | | |

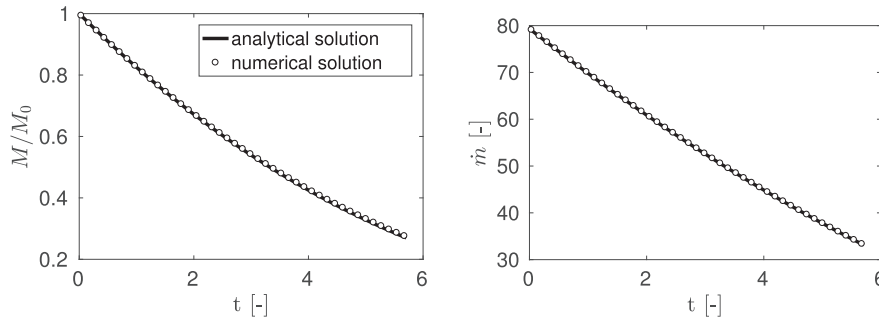


Fig. 5. Evolution of the droplet mass (left panel) and non dimensional vapour flowrate (right panel) for a droplet evaporating at constant radius regression speed.

The analytical expressions for the vapour flowrate at the surface and the droplet mass evolution are:

$$\dot{m} = -4\pi(r_{s0} - ct)^2 c (1 - \phi_\rho). \quad (25)$$

$$M(t) = \frac{4}{3}\pi\phi_\rho(r_{s0} - ct)^3. \quad (26)$$

These are compared in Fig. 5 with the droplet mass evolution and the vapour flowrate through the surface of an arbitrary envelope surrounding the droplet from the numerical simulation. The data show that the error for the vapour flowrate and the droplet mass is within 0.1%.

4.2. Case 2. Free evaporation of a static droplet

Using the same setup as in the previous case, we allow the evaporation rate of the droplet to be determined by the energy and mass transport. The parameters chosen for the problem correspond to n-heptane evaporating in a nitrogen environment, hence an extended Antoine correlation for n-heptane was used as vapour pressure relation [42].

This problem has an asymptotic solution when the heat and species transport in the gas reach steady state, namely:

$$u_r(r, t) = -\frac{\ln(1 + B_M)}{ReSc} \left(\frac{1 - \phi_\rho}{\phi_\rho} \right) \frac{r_s}{r^2}; \quad (27)$$

$$Y(r, t) = 1 - (1 - Y_s)g(r); \quad (28)$$

$$T(r, t) = T_s + (T_\infty - T_s) \frac{F(g(r))}{B_T}; \quad (29)$$

$$B_M = \frac{Y_s - Y_\infty}{1 - Y_s}; \quad (30)$$

$$B_T = F(g(\infty)); \quad (31)$$

$$g(r) = (1 + B_M)^{1 - r_s/r}; \quad (32)$$

$$F(g) = \frac{1}{Le} \int_1^g \xi^{(1/Le)-1} \exp\left(\frac{\phi_{\Delta c_p}}{Le} (1 - Y_s)(\xi - 1)\right) d\xi. \quad (33)$$

Fig. 6, demonstrates that the numerical method is able to capture the coupling of the three transport mechanisms and correctly predict the asymptotic velocity, temperature and species mass fraction fields. The mass fraction profile shows a slight deviation from the asymptotic profile, which can be explained by the fact that the Lewis number is around $Le \approx 2$. This means that the species concentration field needs approximately twice the time to reach its asymptotic value than the temperature field.

4.3. Case 3. Migration of a near-wall droplet by vaporization

Next, we consider the case of a droplet that evaporates in an initially quiescent environment and is positioned near a wall. This configuration is inspired by the case tested by Tanguy et al. [15], who use a Level Set method in a 2D axisymmetric configuration to tackle the problem. The Clausius-Clapeyron relation for water was used as vapour-liquid equilibrium. The vapour ejected by the droplet towards the wall originates an asymmetric pressure gradient that has the effect of a net thrust, pushing the droplet away from the wall (along the y direction in our case). This is illustrated by the snapshots of the velocity field at four subsequent times in Fig. 7.

A grid convergence study with the global mass conservation as the target parameter was also performed. Five Eulerian grids were analysed: $L_x = (64, 96, 128, 144, 256)\Delta x$, which correspond to (16, 24, 32, 36, 64) points per initial droplet diameter. We expect the convergence to be first order as a result of the approximation of gradients at the surface (Eq. (21)). This is verified in Fig. 8b. Fig. 8a shows that for a grid of moderate refinement, corresponding to 32 points per initial droplet diameter, the error in mass is around 3.8%⁶ after the droplet has lost half of its mass.

4.4. Case 4. Evaporation of a hydrocarbon droplet in homogeneous isotropic turbulence

Turbulent transport enhances the evaporation rate by two main mechanisms: displacing more efficiently the vapour away from the droplet surface, and decreasing the thickness of the vapour mass fraction boundary layer at the droplet surface, thus increasing the evaporation driving force [2]. Birouk et al. [43] and Birouk and Gökalp [44] carried out an extensive experimental investigation of the evaporation of hydrocarbon droplets in homogeneous isotropic turbulence with zero mean flow. In their setup, the desired turbulent field is obtained in a cubic chamber with eight fans mounted on the cube corners, pointing towards the centre of the chamber. The droplet (1.5 mm initial diameter) is suspended at the centre of the chamber with a quartz fiber (0.2 mm in diameter). Here we validate our numerical method for turbulent evaporation by reproducing some of the experimental results for n-heptane and n-decane.

Birouk and Gökalp [44] report the statistics (root mean square of the velocity fluctuation, integral, Taylor and Kolmogorov scales) of the turbulence in the evaporation chamber, which is modulated by varying the speed of the eight fans. In order to reproduce as close as possible the same conditions, we employ a cubic box with periodic boundary conditions for pressure and velocity, and force the turbulence in Fourier space with the scheme proposed by

⁶ The error is calculated relative to the Richardson extrapolation based on the three finest grids.

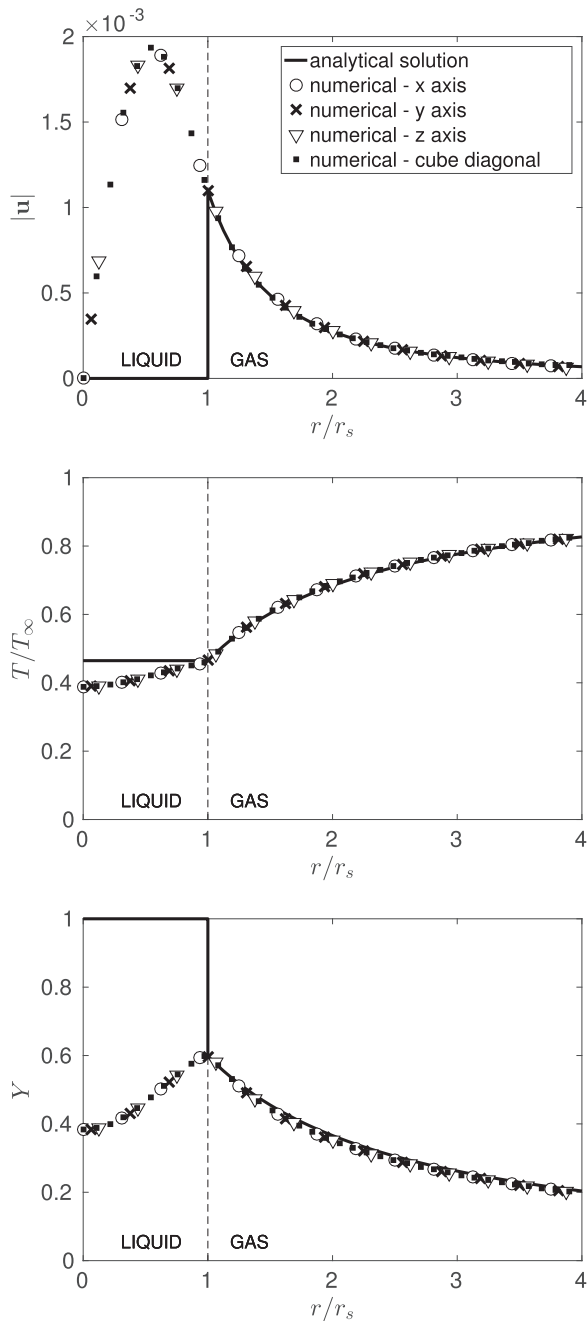


Fig. 6. Asymptotic profiles generated by a static n-heptane droplet evaporating in nitrogen. Velocity magnitude (top panel), non dimensional temperature (middle panel) and n-heptane mass fraction (bottom panel).

Eswaran and Pope [45]. We vary the amplitude of the turbulent forcing to match the turbulent statistics for four experimental data sets, which correspond to fan speeds of 2700, 2270, 1800, 1450 rpm, and are referred to in the following as cases 4a, 4b, 4c and 4d respectively. The droplet position is fixed at the centre of the computational box. Dirichlet boundary conditions of constant ambient temperature and zero vapour mass fraction are imposed on the outer boundaries in order to provide a continuous source of heat and sink of vapour. The droplet temperature is initialized at the wet bulb temperature of the evaporating species, in equilibrium with ambient temperature at atmospheric pressure, assuming that the surrounding gas is nitrogen. Fig. 9 illustrates the computational configuration and a snapshot of the vapour mass fraction and velocity fields.

The quality criteria for the numerical method are established by the ability to reproduce accurately the experimental values for the turbulent statistics (we choose here the turbulent kinetic energy K and the Kolmogorov scale η) and for the droplet evaporation rate, defined as the rate of change of the droplet square diameter $\frac{d(d_s^2)}{dt}$. Table 3 shows, for cases 4a, 4b, 4c and 4d, the comparison between the turbulence statistics and the asymptotic evaporation rate from the experiments and the simulation results, reporting the relative error. The turbulent forcing employed is shown to adequately simulate the experimental conditions. The experimental evaporation rate is calculated from the time variation of the equivalent droplet diameter, which in turn is deduced from the projected surface area of the droplet provided by the experimental image acquisition tool [43,44]. It is evident that droplet deformation can introduce considerable uncertainty in the measurement of the evaporation rate. Birouk and Fabbro [46] show in their Fig. 6b that, for a very similar experiment, the shape distortion caused by the interaction of the turbulent velocity field with the droplet supporting fiber can be significant. Despite these limitations, the discrepancy between experiment and simulation for the evaporation rate, as reported in Table 3, is almost always lower than 10%. This provides a solid validation for the numerical method, and also justifies the sphericity Assumption A4 even under conditions where the shape deformation is not negligible, but the specific surface area does not change much, as already stated in Section 2.1. We also note that the error in the evaporation rate is higher for decane than for heptane, due to the lower volatility of decane, which also leads to a much longer evaporation time.

In Fig. 10 we display the evolution of the normalized droplet surface and of the surface evaporation rate for the n-heptane and n-decane, case 4a. We note that, for the same turbulence intensity, the n-heptane evaporation rate fluctuation is much stronger, due to the higher volatility of the substance.

Finally, we report in Table 4 the average Nusselt and Sherwood numbers, calculated directly from the heat and mass transfer rates. The values fall in the typical range encountered in spray combustion applications.

5. Conclusions and outlook

We have presented an Immersed Boundary Method for incompressible flows with a dispersed phase undergoing phase change. We have shown that the method is able to capture the relevant interplay of mass, momentum and energy transport in the continuous phase and their exchange with the dispersed phase, allowing correct predictions of the global evolution of the system. The method is able to do so without direct solution of the fields inside the dispersed phase, and assuming a priori the interface shape, thus neglecting its deformation. Thanks to these features the method is characterized by higher robustness and lower computational cost compared to other methods that rely on the full solution of the multiphase system (e.g. Volume of Fluid, Level Set, Front Tracking). This is particularly attractive for simulations of applications (e.g. vaporizing sprays) with a dispersed phase whose characteristic size is relatively small, so that on the one hand the details of the transport inside the dispersed phase are negligible, and on the other hand a fully resolved calculation of the heat, mass and momentum exchange with the continuous phase and their transport therein is necessary to correctly reproduce the nonlinear physics. An example of such a case is the first direct numerical simulation, performed by the authors, of a turbulent channel flow with more than 14000 evaporating droplets [47], relying on the method described in the present paper. As shown in [47], the modulation of the continuous phase turbulence by the droplets, and the associated droplet migration, strongly affect the evaporation

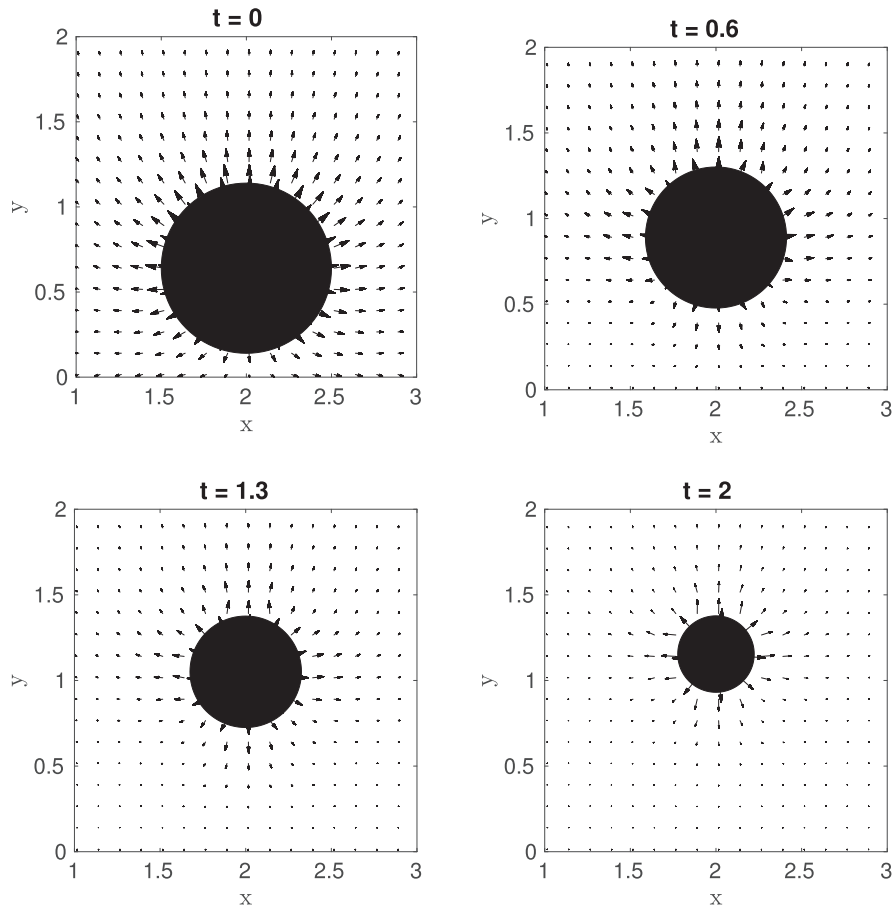


Fig. 7. Velocity fields in the XY plane (at $Z = 0.5L_z$) at four subsequent times. For clarity velocity vectors are not in scale.

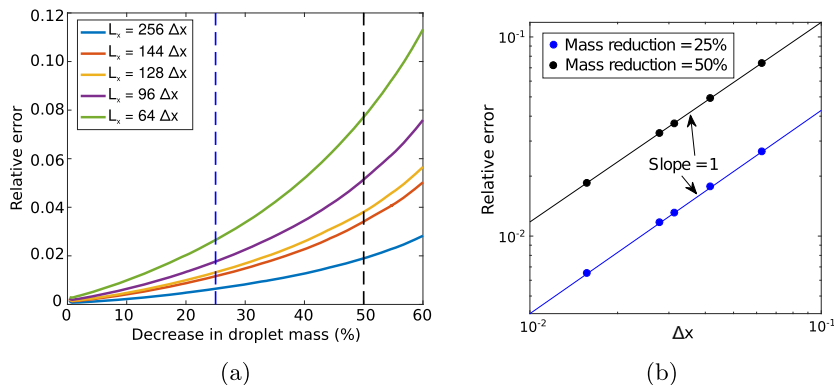


Fig. 8. Grid convergence study. (a) Mass conservation error over time for various grid resolutions, as a function of the percentage reduction of droplet mass. The blue and black dashed lines represent 25% and 50% mass reduction respectively. (b) Order of accuracy for two points in time corresponding to 25% and 50% decrease in droplet mass.

dynamics. As Lagrangian Particle Tracking with modelling of the hydrodynamic forces and phase change related to the dispersed phase is currently the state of art for the numerical simulation of spray evaporation, we believe that the present DNS/IBM method is able to provide relevant physical insight with the aim of improving existing LPT models. Future development of the present method will focus on the treatment of multispecies phase change and complex thermodynamics (non-ideal liquid and gas mixtures). At the same time, there is still considerable room for improvement in developing suitable IBM strategies for cases such as very large liquid-gas density ratios, flows at very high Reynolds number, and extremely fast phase change rates, all instances where the quality of the solution is known to deteriorate.

Improvement of the parallel efficiency is also an open challenge for multiphase IBM solvers [48]. The coupled Lagrangian-Eulerian description of the fluid-fluid interface involves the crossing of multiple subdomains by the moving lagrangian grid. This complicates considerably the communication between tasks, in the presence of phase change that is handled via global phase mass and energy balances, like in our method. Therefore more work is desirable towards better parallel efficiency.

Declaration of Competing Interest

The authors declared that there is no conflict of interest.

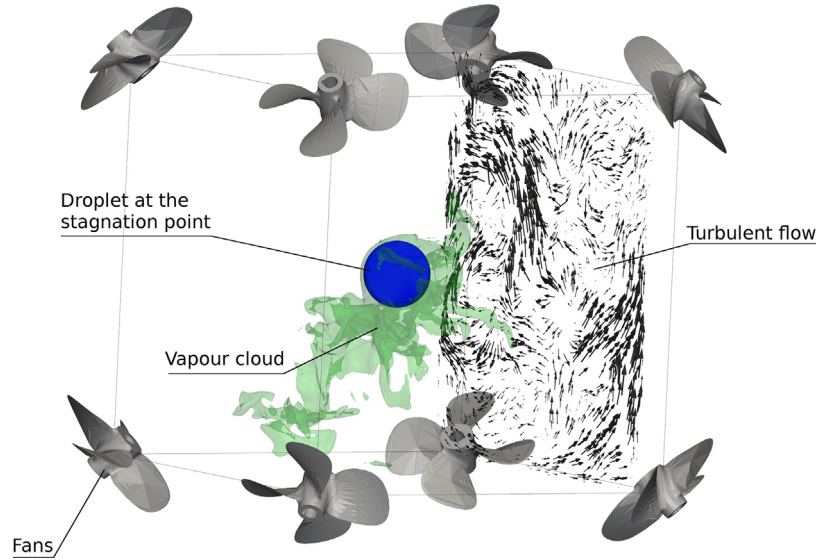


Fig. 9. Evaporation of a droplet in homogeneous isotropic turbulence, case 4. The contour of vapour mass fraction equal to 0.2 is shown around the evaporating droplet. Velocity vectors of the turbulent flow field are shown on a plane. The eight fans are shown as a reference to the experimental setup of Birouk et al. [43] and Birouk and Gökalp [44], but are not included in the numerical model.

Table 3

Comparison between the present work and the experiments of Birouk et al. [43] and Birouk and Gökalp [44]. Values obtained in the present work are indicated in italics next to the experimental values, and the relative error is indicated in parentheses.

| Case | 4a | 4b | 4c | 4d |
|--|---------------------------|--------------------------|---------------------------|---------------------------|
| K [m^2/s^2] | 1.45 <i>1.50</i> (+3.5%) | 0.85 <i>0.79</i> (-6.7%) | 0.58 <i>0.59</i> (+1.7%) | 0.36 <i>0.37</i> (+2.3%) |
| η [mm] | 0.08 <i>0.076</i> (-5%) | 0.10 <i>0.096</i> (-4%) | 0.11 <i>0.108</i> (-1.8%) | 0.13 <i>0.128</i> (-1.5%) |
| $\frac{d(d_p^2)}{dt}$ _{heptane} [$10^{-2} \text{ mm}^2/\text{s}$] | 5.22 <i>5.23</i> (+0.2%) | 4.81 <i>4.66</i> (-3.1%) | 4.35 <i>4.68</i> (+7.6%) | 3.94 <i>4.20</i> (+6.6%) |
| $\frac{d(d_p^2)}{dt}$ _{decane} [$10^{-2} \text{ mm}^2/\text{s}$] | 0.39 <i>0.35</i> (-10.3%) | 0.34 <i>0.31</i> (-8.8%) | 0.28 <i>0.30</i> (+7.1%) | 0.24 <i>0.28</i> (+16.7%) |

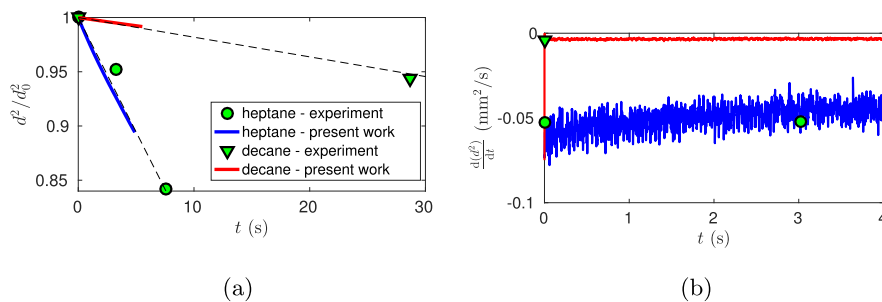


Fig. 10. Evolution of the normalized droplet surface area (a) and evaporation rate (b). Experimental data from [43,44]. Dashed lines represent the least squares regression of the experimental data points.

Table 4

Nusselt and Sherwood numbers for droplet evaporation in homogeneous isotropic turbulence.

| Case | 4a | 4b | 4c | 4d |
|-----------------------|------|------|------|-----|
| Nu_{heptane} | 17.6 | 9.3 | 8.9 | 6.5 |
| Nu_{decane} | 17.4 | 14.8 | 9.6 | 7.1 |
| Sh_{heptane} | 20.9 | 15.5 | 10.6 | 7.7 |
| Sh_{decane} | 21.4 | 14.6 | 10.5 | 7.5 |

Acknowledgements

The work was supported by the Swedish Research Council (VR). Computer time provided by the Swedish National Infrastructure for Computing (project No. SNIC 2018/1-23) and the National

Infrastructure for High Performance Computing and Data Storage in Norway (project No. NN9561K) is acknowledged.

Appendix A. Derivation of the energy transport equation for a multicomponent fluid

The equations in the following appendices are dimensional: for convenience of exposition we therefore remove the “ \wedge ” symbol used until now to denote dimensional quantities.

The energy equation in a multicomponent incompressible system, neglecting viscous heating, is (see Bird et al. [49]):

$$\rho \frac{Dh}{Dt} = -\nabla \cdot \mathbf{q}; \quad (\text{A.1})$$

where $\frac{D}{Dt}$ is the material derivative, $h = \frac{H}{M}$ is the enthalpy per unit mass of the system, \mathbf{q} is the diffusive heat flux.

The specific enthalpy h is an intensive property and therefore depends on the local temperature and composition of the system (pressure dependence is ruled out by the incompressibility assumption). Composition is uniquely determined by a set of $(N - 1)$ independent mass fractions, where N is the number of the system components. Thus:

$$\rho \frac{Dh}{Dt} = \rho \left(\frac{\partial h}{\partial T} \right)_{Y_i} \frac{DT}{Dt} + \rho \sum_{j=1}^{N-1} \left(\frac{\partial h}{\partial Y_j} \right)_{T, Y_{i \neq j}} \frac{DY_j}{Dt}. \quad (\text{A.2})$$

Since $H = hM = h \sum_{j=1}^N M_j$, the variation of the total enthalpy with the mass of each component is:

$$\left(\frac{\partial H}{\partial M_k} \right)_{M_{i \neq k}} = h + \sum_{j=1}^{N-1} \left(\frac{\partial h}{\partial Y_j} \right)_{T, Y_{i \neq j}} (\delta_{jk} - Y_j); \quad \text{for } k \neq N; \quad (\text{A.3a})$$

$$\left(\frac{\partial H}{\partial M_k} \right)_{M_{i \neq k}} = h + \sum_{j=1}^{N-1} \left(\frac{\partial h}{\partial Y_j} \right)_{T, Y_{i \neq j}} (-Y_j); \quad \text{for } k = N. \quad (\text{A.3b})$$

Subtracting Eq. (A.3b) from Eq. (A.3a) we get:

$$\left(\frac{\partial h}{\partial Y_{k \neq N}} \right)_{T, Y_{i \neq k}} = \left(\frac{\partial H}{\partial M_{k \neq N}} \right)_{M_{i \neq k}} - \left(\frac{\partial H}{\partial M_N} \right)_{M_{i \neq N}}. \quad (\text{A.4})$$

Now the partial molar enthalpy of species k is defined as $\tilde{h}_k = \left(\frac{\partial H}{\partial n_k} \right)_{T, n_{i \neq k}}$, where n_k is the number of moles of k in the system.

Therefore $H = \sum_{j=1}^N \tilde{h}_j n_j$, and the partial mass enthalpy is:

$$\left(\frac{\partial H}{\partial M_k} \right)_{M_{i \neq k}} = \frac{\tilde{h}_k}{M_{w,k}}. \quad (\text{A.5})$$

The variation of the specific mass enthalpy with temperature is obviously the specific mass heat capacity:

$$\left(\frac{\partial h}{\partial T} \right)_{Y_i} = c_p. \quad (\text{A.6})$$

Substituting Eq. (A.5) into Eq. (A.4) and using the latter, together with Eq. (A.6), in Eq. (A.2), gives:

$$\rho \frac{Dh}{Dt} = \rho c_p \frac{DT}{Dt} + \rho \sum_{j=1}^{N-1} \left(\frac{\tilde{h}_j}{M_{w,j}} - \frac{\tilde{h}_N}{M_{w,N}} \right) \frac{DY_j}{Dt}. \quad (\text{A.7})$$

Using the transport equation for the mass fraction of k :

$$\rho \frac{DY_k}{Dt} = -\nabla \cdot \mathbf{j}_k; \quad (\text{A.8})$$

where \mathbf{j}_k is the diffusive flux of species k , and the fact that $\sum_{j=1}^N Y_j = 1$ so that $\sum_{j=1}^{N-1} \mathbf{j}_j = -\mathbf{j}_N$, Eq. (A.7) can be rewritten as:

$$\rho \frac{Dh}{Dt} = \rho c_p \frac{DT}{Dt} - \sum_{j=1}^N \left(\frac{\tilde{h}_j}{M_{w,j}} \right) \nabla \cdot \mathbf{j}_j. \quad (\text{A.9})$$

In the absence of Dufour effect, the diffusive heat flux is the sum of heat conduction and enthalpy transport due to species diffusion:

$$\mathbf{q} = -k \nabla T + \sum_{j=1}^N \left(\frac{\tilde{h}_j}{M_{w,j}} \right) \mathbf{j}_j. \quad (\text{A.10})$$

Using Eqs. (A.9) and (A.10), Eq. (A.1) can be rewritten as:

$$\rho c_p \frac{DT}{Dt} = k \nabla^2 T - \sum_{j=1}^N \left(\frac{\nabla \tilde{h}_j}{M_{w,j}} \right) \cdot \mathbf{j}_j. \quad (\text{A.11})$$

By the assumption of ideal gas mixture, there is no excess heat of mixing, and the total enthalpy of the system is the sum of the pure enthalpies of its components:

$$H = \sum_{j=1}^N n_j \tilde{h}_j = \sum_{j=1}^N H_{j,pure}(T, n_j) = \sum_{j=1}^N n_j \tilde{c}_{p,j} (T - T_{ref}). \quad (\text{A.12})$$

Finally, we use Eq. (A.12) and Fick's law for \mathbf{j}_k in Eq. (A.11), to obtain

$$\rho c_p \frac{DT}{Dt} = k \nabla^2 T + \rho \sum_{j=1}^N c_{p,j} D_{j,mix} \nabla T \cdot \nabla Y_j; \quad (\text{A.13})$$

where $D_{k,mix}$ is the binary diffusivity of component k into the mixture.

Appendix B. Heating/cooling of a sphere

Consider the heating/cooling of a sphere through the surface boundary condition.

With the assumption of constant heat diffusivity α , the problem is described by the spherical heat equation with initial and boundary conditions:

$$\begin{aligned} \frac{1}{\alpha} \frac{\partial T}{\partial t} &= \frac{1}{r^2} \frac{\partial}{\partial r} \left(r^2 \frac{\partial T}{\partial r} \right); \\ \left. \frac{\partial T}{\partial r} \right|_{r=0} &= 0; \\ T(r = r_s, t) &= T_s(t); \\ T(r, t = 0) &= T_0(r). \end{aligned} \quad (\text{B.1})$$

In order to find an analytical solution, let us assume that the boundary condition changes slowly, so that we can define $\theta(r, t) = T(t) - T_s(t)$, and drop the unsteady term $\frac{dT_s}{dt}$. The resulting homogeneous initial value problem is:

$$\begin{aligned} \frac{1}{\alpha} \frac{\partial \theta}{\partial t} &= \frac{1}{r^2} \frac{\partial}{\partial r} \left(r^2 \frac{\partial \theta}{\partial r} \right); \\ \left. \frac{\partial \theta}{\partial r} \right|_{r=0} &= 0; \\ \theta(r = r_s, t) &= 0; \\ \theta(r, t = 0) &= \theta_0(r); \end{aligned} \quad (\text{B.2})$$

which we can solve by separation of variables. The substitution $\theta(r, t) = \phi(r)\psi(t)$ gives two ODEs:

$$\frac{1}{\psi} \frac{d\psi}{dt} = -\alpha \lambda^2; \quad (\text{B.3})$$

$$\frac{1}{\phi} \frac{1}{r^2} \frac{d}{dr} \left(r^2 \frac{d\phi}{dr} \right) = -\lambda^2. \quad (\text{B.4})$$

The constant $(-\lambda^2)$ is negative because the temperature must asymptotically relax to the boundary value T_s . The solution to Eq. (B.3) is:

$$\psi = C e^{-\alpha \lambda^2 t}. \quad (\text{B.5})$$

Eq. (B.4) can be rewritten as:

$$\frac{d^2}{dr^2} (r\phi) + \lambda^2 (r\phi) = 0; \quad (\text{B.6})$$

which is a linear second order ODE with constant coefficients and solution:

$$\phi = C_1 \frac{\sin(\lambda r)}{r} + C_2 \frac{\cos(\lambda r)}{r}. \quad (\text{B.7})$$

Since the solution must be finite at $r = 0$, $C_2 = 0$ (the symmetry condition at the centre $\left. \frac{d\phi}{dr} \right|_{r=0} = 0$ is then identically satisfied).

By applying the boundary condition at the surface we find that (remembering that $\lambda \neq 0$):

$$\lambda = \lambda_n = \frac{n\pi}{r_s}; \quad \text{for } n = 1, 2, \dots \quad (\text{B.8})$$

Therefore the general solution to Problem (B.2) is:

$$\theta(r, t) = \sum_{n=1}^{\infty} \frac{A_n}{r} \sin(\lambda_n r) e^{-\alpha \lambda_n^2 t}. \quad (\text{B.9})$$

To find the coefficients A_n we apply the initial condition:

$$\theta_0(r) = \sum_{n=1}^{\infty} \frac{A_n}{r} \sin(\lambda_n r); \quad (\text{B.10})$$

i.e. the initial condition is represented by a sine series whose coefficients are:

$$A_n = \frac{2}{r_s} \int_0^{r_s} r \theta_0(r) \sin(\lambda_n r) dr. \quad (\text{B.11})$$

If the initial condition is uniform $\theta_0(r) = \theta_0$, then:

$$A_n = -2\theta_0 r_s \frac{(-1)^n}{n\pi}. \quad (\text{B.12})$$

Appendix C. Supplementary material

Supplementary data associated with this article can be found, in the online version, at <https://doi.org/10.1016/j.ijheatmasstransfer.2019.118563>.

References

- [1] L.D. Eskin, M.M. Molton, B.A. Turner, R.G. Joklik, M.S. Klassen, R.G. Roby, Long-term demonstration of a lean, premixed, prevaporized (LPP) system for gas turbines, in: Proceedings of the 20th International Conference on Nuclear Engineering, 2012.
- [2] B. Abramzon, W.A. Sirignano, Droplet vaporization model for spray combustion calculations, *Int. J. Heat Mass Transf.* 32 (9) (1989) 1605–1618.
- [3] S.S. Sazhin, Advanced models of fuel droplet heating and evaporation, *Prog. Energy Combust. Sci.* 32 (2) (2006) 162–214.
- [4] R.J. Kee, K. Yamashita, H. Zhu, A.M. Dean, The effects of liquid-fuel thermophysical properties, carrier-gas composition, and pressure, on strained opposed-flow non-premixed flames, *Combust. Flame* 158 (6) (2011) 1129–1139.
- [5] M. Mezhericher, A. Levy, I. Borde, Spray drying modelling based on advanced droplet drying kinetics, *Chem. Eng. Process.* 49 (2010) 1205–1213.
- [6] Y. Feng, C. Kleinstreuer, A. Rostami, Evaporation and condensation of multicomponent electronic cigarette droplets and conventional cigarette smoke particles in an idealized G3-G5 triple bifurcating unit, *J. Aerosol Sci.* 80 (2015) 58–74.
- [7] A. Liñan, D. Martínez-uiz, A.L. Sánchez, J. Urzay, Regimes of spray vaporization and combustion in counterflow configurations, *Combust. Sci. Technol.* 187 (1–2) (2015) 103–131.
- [8] G. Ryskin, L.G. Leal, Numerical solution of free-boundary problems in fluid mechanics. Part 1. The finite-difference technique, *J. Fluid Mech.* 148 (1984) 1–17.
- [9] M. Renksizbulut, M.C. Yuen, Numerical study of droplet evaporation in a high-temperature stream, *ASME J. Heat Trans.* 105 (2) (1983) 389–397.
- [10] S.O. Unverdi, G. Tryggvason, A front-tracking method for viscous, incompressible, multi-fluid flows, *J. Comput. Phys.* 100 (1) (1992) 25–37.
- [11] D. Juric, G. Tryggvason, Computations of boiling flows, *Int. J. Multiph. Flow* 24 (1998) 387–410.
- [12] S.W.J. Welch, J. Wilson, A volume of fluid based method for fluid flows with phase change, *J. Comput. Phys.* 160 (2000) 662–682.
- [13] J. Schlotke, B. Weigand, Direct numerical simulation of evaporating droplets, *J. Comput. Phys.* 227 (2008) 5215–5237.
- [14] D.Q. Nguyen, R.P. Fedkiw, M. Kang, A boundary condition capturing method for incompressible flame discontinuities, *J. Comput. Phys.* 172 (2001) 71–98.
- [15] S. Tanguy, T. Ménard, A. Berlemont, A level set method for vaporizing two-phase flows, *J. Comput. Phys.* 221 (2007) 837–853.
- [16] R. Ledesma-Aguilar, D. Vella, J.M. Yeomans, Lattice-Boltzmann simulations of droplet evaporation, *Soft Matter* 10 (41) (2014) 8267–8275.
- [17] D. Albernaz, M. Do-Quang, G. Amberg, Multirelaxation-time lattice Boltzmann model for droplet heating and evaporation under forced convection, *Phys. Rev. E* 91 (4) (2015) 043012–1–043012-11.
- [18] D.M. Anderson, G.B. McFadden, A.A. Wheeler, Diffuse-interface methods in fluid mechanics, *Annu. Rev. Fluid Mech.* 30 (1998) 139–165.
- [19] A. Lamorgese, R. Mauri, Modeling soft interface dominated systems: a comparison of phase field and Gibbs dividing surface models, *Phys. Rep.* 675 (2017) 1–54.
- [20] C.S. Peskin, The immersed boundary method, *Acta Numerica* 11 (2002) 479–517.
- [21] R. Mittal, G. Iaccarino, Immersed boundary methods, *Annu. Rev. Fluid Mech.* 37 (2005) 239–261.
- [22] M. Uhlmann, An immersed boundary method with direct forcing for the simulation of particulate flows, *J. Comput. Phys.* 209 (2005) 448–476.
- [23] W.P. Breugem, A second-order accurate immersed boundary method for fully resolved simulations of particle-laden flows, *J. Comput. Phys.* 231 (2012) 4469–4498.
- [24] I. Lashgari, F. Picano, W.P. Breugem, L. Brandt, Laminar, turbulent, and inertial shear-thickening regimes in channel flow of neutrally buoyant particle suspensions, *Phys. Rev. Lett.* 113 (2014) 254502–1–254502-5.
- [25] F. Picano, W.P. Breugem, L. Brandt, Turbulent channel flow of dense suspensions of neutrally buoyant spheres, *J. Fluid Mech.* 764 (2015) 463–487.
- [26] P. Costa, F. Picano, L. Brandt, W.P. Breugem, Universal scaling laws for dense particle suspensions in turbulent wall-bounded flows, *Phys. Rev. Lett.* 113 (2016) 134501–1–134501-5.
- [27] M.N. Ardekani, L.A. Asmar, F. Picano, L. Brandt, Numerical study of heat transfer in laminar and turbulent pipe flow with finite-size spherical particles, *Int. J. Heat Fluid Flow* 71 (2018) 189–199.
- [28] G.L. Hubbard, V.E. Denny, A.F. Mills, Droplet evaporation: effects of transients and variable properties, *Int. J. Heat Mass Transf.* 18 (9) (1975) 1003–1008.
- [29] R. Kneer, M. Schneider, B. Noll, S. Wittig, Effects of variable liquid properties on multicomponent droplet vaporization, *ASME J. Eng. Gas Turb. Power* 115 (3) (1993) 467–472.
- [30] G. Lupo, C. Duwig, A numerical study of ethanol-water droplet evaporation, *ASME, J. Eng. Gas Turbines Power* 140 (2) (2017) 021401–1–021401-9.
- [31] W. Fornari, F. Picano, L. Brandt, Sedimentation of finite-size spheres in quiescent and turbulent environments, *J. Fluid Mech.* 788 (2016) 640–669.
- [32] C.K. Law, Internal boiling and superheating in vaporizing multicomponent droplets, *AIChE J.* 24 (4) (1978) 626–632.
- [33] M. Pilch, C.A. Erdman, Use of breakup time data and velocity history data to predict the maximum size of stable fragments for acceleration-induced breakup of a liquid drop, *Int. J. Multiph. Flow* 13 (6) (1987) 741–757.
- [34] J.L.H. Sallevelt, A.K. Pozarlik, M. Beran, L.-U. Axelsson, G. Brem, Bioethanol combustion in an industrial gas turbine combustor: simulations and experiments, *ASME, J. Eng. Gas Turbines Power* 136 (7) (2014) 071501–1–071501-8.
- [35] V. Ebrahimi, C. Habchi, Towards a predictive evaporation model for multicomponent hydrocarbon droplets at all pressure conditions, *Int. J. Heat Mass Transf.* 54 (2011) 3552–3565.
- [36] S.R. de Groot, P. Mazur, *Non-equilibrium thermodynamics*, chap. 11, Heat conduction, diffusion and cross-effects, Dover, New York, NY, USA, 1984.
- [37] R.S. Volkov, P.A. Strizhak, Research of temperature fields and convection velocities in evaporating water droplets using Planar Laser-Induced Fluorescence and Particle Image Velocimetry, *Exp. Thermal Fluid Sci.* 97 (2018) 392–407.
- [38] D.D. Joseph, Y.Y. Renardy, *Fundamentals of two-fluid dynamics. Part I: Mathematical theory and applications*, Springer, New York, NY, USA, 1993.
- [39] O.V. Vysokomornaya, G.V. Kuznetsov, P.A. Strizhak, Evaporation of water droplets in a high-temperature gaseous medium, *J. Eng. Phys. Thermophys.* 89 (1) (2016) 141–151.
- [40] L.R. Villegas, R. Alis, M. Lepilliez, S. Tanguy, A ghost fluid/level set method for boiling flows and liquid evaporation: application to the Leidenfrost effect, *J. Comput. Phys.* 316 (2016) 789–813.
- [41] A.M. Roma, C.S. Peskin, M.J. Berger, An adaptive version of the immersed boundary method, *J. Comput. Phys.* 153 (1999) 509–534.
- [42] D.W. Green, R.H. Perry, *Perry's Chemical Engineers' Handbook*, McGraw-Hill, Columbus, OH, USA, 2007.
- [43] M. Birouk, C. Chauveau, B. Sarh, A. Quilgars, I. Gökalp, Turbulence effects on the vaporization of monocomponent single droplets, *Combust. Sci. Technol.* 113 (1) (1996) 413–428.
- [44] M. Birouk, I. Gökalp, A new correlation for turbulent mass transfer from liquid droplets, *Int. J. Heat Mass Transf.* 45 (1) (2002) 37–45.
- [45] V. Eswaran, S.B. Pope, An examination of forcing in direct numerical simulations of turbulence, *Comput. Fluids* 16 (3) (1988) 257–278.
- [46] M. Birouk, S.C. Fabbro, Droplet evaporation in a turbulent atmosphere at elevated pressure - Experimental data, *Proc. Combust. Inst.* 34 (1) (2013) 1577–1584.
- [47] C. Duwig, G. Lupo, A. Gruber, L. Brandt, P.B. Govindaraju, T. Jaravel, M. Ihme, Direct numerical simulation, analysis, and advanced modeling of the evaporation of multiple fuel droplets in a hot turbulent flow, in: Proceedings of the Summer Program 2018, Center for Turbulence Research, Stanford University, 2018, pp. 319–328.
- [48] W.X. Huang, F.B. Tian, Recent trends and progresses in the immersed boundary method, *Proc. Instit. Mech. Eng. C: J. Mech. Eng. Sci.* (2019) 1–20.
- [49] R.B. Bird, W.E. Stewart, E.N. Lightfoot, *Transport Phenomena*, chap. 19, Equations of change for multicomponent systems, John Wiley & Sons, New York, NY, USA, 2007.